



SOLIS IV. Hydrocarbons in the OMC-2 FIR4 Region, a Probe of Energetic Particle Irradiation of the Region*

C. Favre^{1,2}, C. Ceccarelli¹, A. López-Sepulcre^{1,3}, F. Fontani², R. Neri³, S. Manigand^{1,4}, M. Kama⁵, P. Caselli⁶, A. Jaber Al-Edhari^{1,7}, C. Kahane¹, F. Alves⁶, N. Balucani⁸, E. Bianchi², E. Caux^{9,10},

C. Codella², F. Dulieu¹¹, J. E. Pineda⁶, I. R. Sims¹², and P. Theulé¹³

¹ Univ. Grenoble Alpes, CNRS, IPAG, F-38000 Grenoble, France; cfavre@arcetri.astro.it

² INAF-Osservatorio Astrofisico di Arcetri, Largo E. Fermi 5, I-50125, Florence, Italy

³ Institut de Radioastronomie Millimétrique, 300 rue de la Piscine, F-38406, Saint-Martin d'Hères, France

⁴ Centre for Star and Planet Formation, Niels Bohr Institute & Natural History Museum of Denmark, University of Copenhagen, Øster Voldgade 5-7, DK-1350 Copenhagen K., Denmark

⁵ Institute of Astronomy, University of Cambridge, Madingley Road, Cambridge CB3 0HA, UK

⁶ Max-Planck-Institut für extraterrestrische Physik, Giessenbachstrasse 1, D-85748 Garching, Germany

⁷ University of AL-Muthanna, College of Science, Physics Department, AL-Muthanna, Iraq

⁸ Dipartimento di Chimica, Biologia e Biotecnologie, Università di Perugia, Via Elce di Sotto 8, I-06123 Perugia, Italy

⁹ Université de Toulouse, UPS-OMP, IRAP, Toulouse, France

¹⁰ CNRS, IRAP, 9 Av. Colonel Roche, BP 44346, F-31028 Toulouse Cedex 4, France

¹¹ LERMA, Université de Cergy-Pontoise, Observatoire de Paris, PSL Research University, CNRS, Sorbonne Université, UPMC Univ. Paris 06, École normale supérieure, France

¹² Institut de Physique de Rennes, UMR CNRS 6251, Université de Rennes 1, 263 Avenue du Général Leclerc, F-35042 Rennes Cedex, France

¹³ Aix-Marseille Université, PIIM UMR-CNRS 7345, F-13397 Marseille, France

Received 2017 October 26; revised 2018 April 16; accepted 2018 April 20; published 2018 June 1

Abstract

We report new interferometric images of cyclopropenylidene, $c\text{-C}_3\text{H}_2$, toward the young protocluster OMC-2 FIR 4. The observations were performed at 82 and 85 GHz with the Northern Extended Millimeter Array (NOEMA) as part of the project Seeds Of Life In Space (SOLIS). In addition, IRAM-30 m data observations were used to investigate the physical structure of OMC-2 FIR 4. We find that the $c\text{-C}_3\text{H}_2$ gas emits from the same region where previous SOLIS observations showed bright HC_5N emission. From a non-LTE analysis of the IRAM-30 m data, the $c\text{-C}_3\text{H}_2$ gas has an average temperature of ~ 40 K, a H_2 density of $\sim 3 \times 10^5 \text{ cm}^{-3}$, and a $c\text{-C}_3\text{H}_2$ abundance relative to H_2 of $(7 \pm 1) \times 10^{-12}$. In addition, the NOEMA observations provide no sign of significant $c\text{-C}_3\text{H}_2$ excitation temperature gradients across the region (about 3–4 beams), with T_{ex} in the range 8 ± 3 up to 16 ± 7 K. We thus infer that our observations are inconsistent with a physical interaction of the OMC-2 FIR 4 envelope with the outflow arising from OMC-2 FIR 3, as claimed by previous studies. The comparison of the measured $c\text{-C}_3\text{H}_2$ abundance with the predictions from an astrochemical PDR model indicates that OMC-2 FIR 4 is irradiated by an FUV field ~ 1000 times larger than the interstellar one, and by a flux of ionizing particles ~ 4000 times larger than the canonical value of $1 \times 10^{-17} \text{ s}^{-1}$ from the Galaxy cosmic rays, which is consistent with our previous HC_5N observations. This provides an important and independent confirmation of other studies that one, or more, source inside the OMC-2 FIR 4 region emits energetic (≥ 10 MeV) particles.

Key words: ISM: abundances – ISM: clouds – ISM: molecules – radio lines: ISM

1. Introduction

Earth is so far the only known place where life is present. Why life emerged and what conditions are essential for that are questions that challenge our knowledge and still represent a mystery. It is very likely that life is the result of a very long and complex process that started as early as the formation of the solar system (hereafter, SS). Sparse traces of the process have been left in the SS small bodies (e.g., Caselli & Ceccarelli 2012), so that to reconstruct it we need (also) to look at places that are forming solar-type planetary systems today. However, finding such systems depends on the partial knowledge that we have of the history of the SS formation. In practice, therefore, reconstructing the SS past history has to be an “iterative” process.

Among the information provided by the mentioned SS left traces, two are particularly relevant for the work presented in this article. First, the Sun was most likely born in a crowded star cluster in the vicinity of high-mass stars, and not in an isolated cloud (e.g., Adams 2010). Second, it underwent a period of intense irradiation from energetic (≥ 10 MeV) particles, even though the cause is not clear yet (e.g., Gounelle et al. 2013).

When taking these two facts into account, the source OMC-2 FIR 4, north of the famous Orion KL region, is so far the best and closest analog of the SS progenitor in our hands. Indeed, available observations show that OMC-2 FIR 4 is a cluster of several young protostars (Shimajiri et al. 2011, 2015; López-Sepulcre et al. 2013b) and that it is permeated by a flux of energetic particles, cosmic-ray (CR) like, which ionize the molecular gas at a rate more than 4000 times the “canonical” value of $1 \times 10^{-17} \text{ s}^{-1}$ in the Galaxy (Ceccarelli et al. 2014; Fontani et al. 2017). Given the vicinity of the Trapezium OB star cluster, the region is also subject to a strong irradiation from FUV photons, about 1000 times larger than the interstellar field (López-Sepulcre et al. 2013a).

* Based on observations carried out under project number L15AA with the IRAM NOEMA Interferometer. IRAM is supported by INSU/CNRS (France), MPG (Germany) and IGN (Spain).

Table 1

Properties of the Cyclopropenylidene ($c\text{-C}_3\text{H}_2$) Lines Observed with the NOEMA Interferometer: Spectroscopic Line Parameters (Transition, Frequency, Upper-level Energy, and Einstein Coefficient) and Major Characteristics of the Observations (Synthesized Beam and P.A.)

Trans.	Freq. (MHz)	E_{up} (K)	A (10^{-5} s^{-1})	Beam ($''$)	P.A. ($^\circ$)
para $c\text{-C}_3\text{H}_2$					
$2_{0,2}-1_{1,1}$	82093.544	6.4	2.1	9.3×5.9	-206
ortho $c\text{-C}_3\text{H}_2$					
$3_{1,2}-3_{0,3}$	82966.197	16.0	1.1	9.3×5.9	-206
$2_{1,2}-1_{0,1}$	85338.896	6.4	2.6	4.7×2.2	14

Note. We used the spectroscopic data parameters from Bogey et al. (1986), Vrtilik et al. (1987), Lovas et al. (1992), and Spezzano et al. (2012), that are available from the Cologne Database for Molecular Spectroscopy molecular line catalog (CDMS, Müller et al. 2005). The Einstein coefficients assume an ortho-to-para ratio of 3:1.

For these reasons, OMC-2 FIR 4 is one of the targets of the project Seeds Of Life In Space (SOLIS; Ceccarelli et al. 2017) whose goal is to understand how molecular complexity grows in Solar-type star-forming systems. Within this project, we carried out observations with the IRAM Northern Extended Millimeter Array (NOEMA) interferometer at various frequencies. A first study on the cyanopolyynes (HC_3N and HC_5N) showed that carbon chains growth is favored in OMC-2 FIR 4, likely thanks to the presence of the large CR-like ionizing particles flux (Fontani et al. 2017).

In this work, we present new SOLIS observations of the small hydrocarbon $c\text{-C}_3\text{H}_2$. The NOEMA SOLIS data are complemented with broadband IRAM-30 m observations at 1–3 mm. The article is organized as follows. Section 2 describes these new observations. We detected and imaged several lines as described in Section 3. With this large and diversified data set, we could carry out a sophisticated analysis of the excitation conditions (Section 4) and the chemical structure (Section 5) of the region. In Section 6, we discuss the information provided by the new observations and the implications on the processes occurring in the OMC-2 FIR 4 region.

2. Observations and Data Reduction

We obtained observations of three $c\text{-C}_3\text{H}_2$ lines with the IRAM interferometer NOEMA within the SOLIS project (Ceccarelli et al. 2017). They are here complemented with IRAM 30 m observations of several $c\text{-C}_3\text{H}_2$ lines, detected in the spectral survey previously carried out toward OMC-2 FIR 4 in the 3, 2, and 1 mm bands (López-Sepulcre et al. 2015). We present the two sets of observations separately.

2.1. SOLIS NOEMA Observations

Three $c\text{-C}_3\text{H}_2$ lines, one para ($2_{0,2}-1_{1,1}$) and two ortho ($3_{1,2}-3_{0,3}$ and $2_{1,2}-1_{0,1}$), were imaged toward OMC-2 FIR 4 with the IRAM NOEMA interferometer. The first two lines, both at ~ 82 GHz, were observed with six antennas on 2015 August 5, 11, 12, 13, and 19 in the D configuration (see also Fontani et al. 2017). The third line, at 85 GHz, was observed with eight antennas on 2016 April 29 and 2016 October 26 in the C configuration. All three lines were observed with the

WideX band correlator, which provides 1843 channels over 3.6 GHz bandwidth with a channel width of 1.95 MHz ($\sim 7.2 \text{ km s}^{-1}$ at 82 GHz). Table 1 reports the spectroscopic data and the main characteristics of the observations.

The phase-tracking center was $\alpha_{J2000} = 05^{\text{h}}35^{\text{m}}26^{\text{s}}.97$, $\delta_{J2000} = -05^{\circ}09'56''.8$ for all data sets, and the systemic velocity of OMC2-FIR4 was set to $V_{\text{LSR}} = 11.4 \text{ km s}^{-1}$. The primary beams are about $61''$ and $59''$ for data at 82 GHz and 85 GHz, respectively. The nearby quasars 3C454.3 and 0524+034 were, respectively, used as bandpass calibrator and gain calibrator for the observations at 82 GHz. Regarding the observations performed at 85 GHz, 0524+024 and 0539-057 were used as gain (phase and amplitude) calibrations, while 3C454.3 was used as a bandpass calibrator. The absolute flux calibration was performed through observations of the quasars LKHA101 (0.21 Jy) for 2015 August 5 and 19, MWC349 (1.03 Jy) for 2015 August 11, 12, and 13 and again MWC349 (1.05 Jy) for 2016 observations.

Continuum subtraction and data imaging were performed using the GILDAS software.¹⁴ The cleaning of the spectral lines was performed by using the Hogbom method (Högbom 1974). The resulting synthesized beam size of the molecular emission maps are $9''.5 \times 6''.1$ (P.A. = -206°) and $4''.7 \times 2''.2$ (P.A. = 14°) at 82 GHz and 85 GHz, respectively. The NOEMA emission maps shown in this paper are corrected for the primary beam.

2.2. IRAM-30 m Observations

Additional observations of the $c\text{-C}_3\text{H}_2$ lines were obtained in the context of the unbiased spectral survey of OMC-2 FIR 4 obtained with the IRAM 30 m telescope. The 3 mm (80.5–116.0 GHz), 2 mm (129.2–158.8 GHz), and 1 mm (202.5–266.0 GHz) bands were observed between 2011 August 31 and 2014 February 7. The Eight Mixer Receiver (EMIR) connected to the 195 kHz resolution about 0.7 km s^{-1} at 83 GHz) Fourier Transform Spectrometer units were used. The main beam sizes are about $9''$ – $12''$, $16''$, and $30''$ at 1, 2, and 3 mm, respectively. The observations were carried out in wobbler switch mode, with a throw of $180''$. Pointing and focus were performed regularly. The coordinates of the IRAM-30 m observations are $\alpha_{J2000} = 05^{\text{h}}35^{\text{m}}26^{\text{s}}.97$ and $\delta_{J2000} = -05^{\circ}09'54''.5$. For further details, see López-Sepulcre et al. (2015).

We used the package CLASS90 of the GILDAS software collection to reduce the data. The uncertainties of calibration are estimated to be lower than 10% at 3 mm and 20% at 2 and 1 mm. After subtraction of the continuum emission via first-order polynomial fitting, a final spectrum was obtained by stitching the spectra from each scan and frequency setting. The intensity was converted from antenna temperature (T_{ant}^*) to main beam temperature (T_{mb}) using the beam efficiencies provided at the IRAM website for the epoch of the observations.

3. Results

3.1. $c\text{-C}_3\text{H}_2$ Emission maps

The NOEMA emission maps of the three $c\text{-C}_3\text{H}_2$ lines integrated over the line profile are shown in Figure 1 (panels (a) to (c)). The figure also displays the continuum emission (panel (d)), previously reported by Fontani et al. (2017), for reference.

¹⁴ <http://www.iram.fr/IRAMFR/GILDAS/>

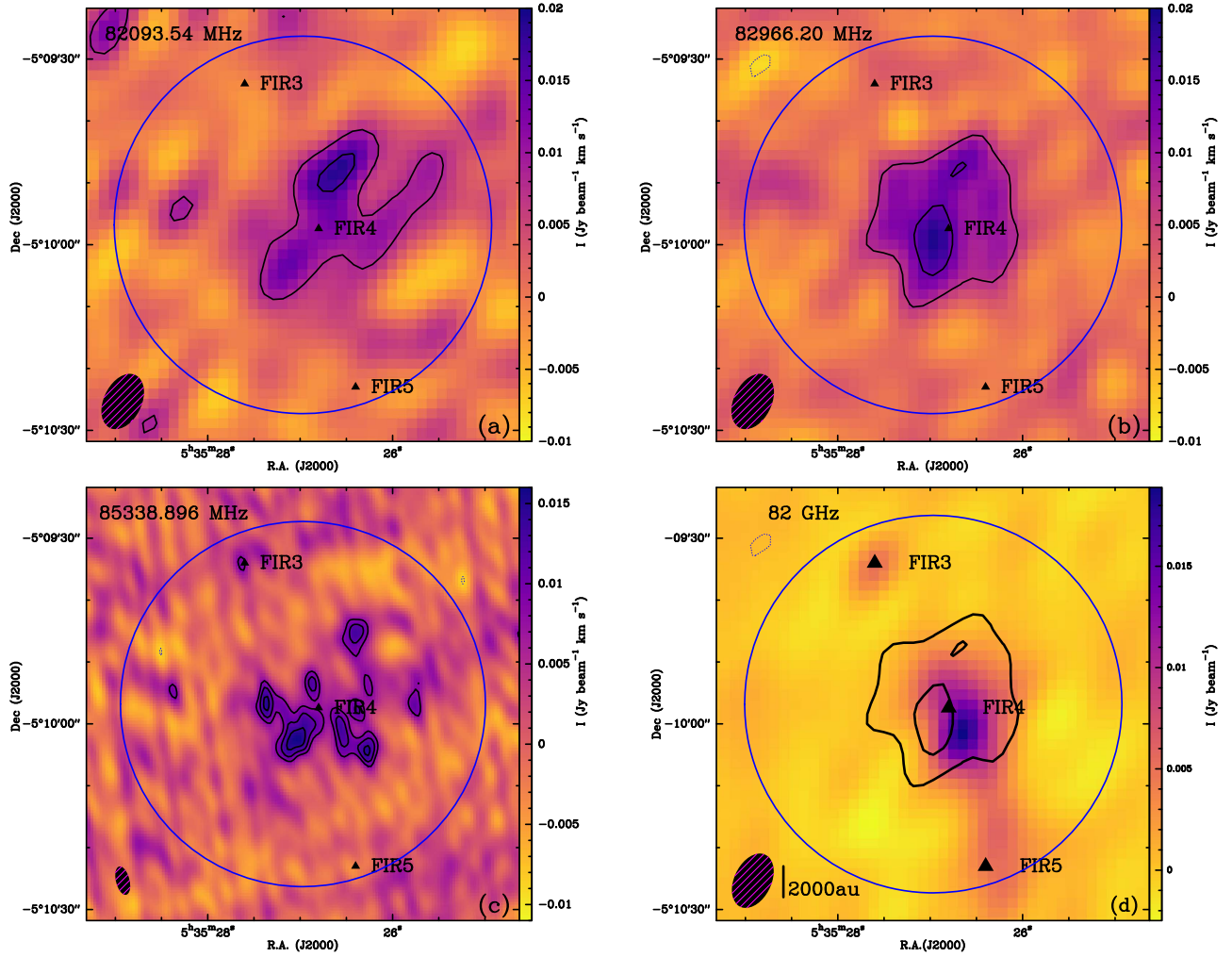


Figure 1. Panel (a): $c\text{-C}_3\text{H}_2$ ($2_{0,2}\text{--}1_{1,1}$) integrated intensity emission map (between 0 and 22 km s^{-1}). The contour levels are at 3σ and 6σ (where $1\sigma = 2.76 \times 10^{-3}\text{ Jy beam}^{-1}\text{ km s}^{-1}$). Panel (b): $c\text{-C}_3\text{H}_2$ ($3_{1,2}\text{--}3_{0,3}$) integrated intensity emission map (between 0 and 22 km s^{-1}). The contour levels are at 3σ and 6σ (where $1\sigma = 2.4 \times 10^{-3}\text{ Jy beam}^{-1}\text{ km s}^{-1}$). Panel (c): $c\text{-C}_3\text{H}_2$ ($2_{1,2}\text{--}1_{0,1}$) integrated intensity emission map (between 0 and 22 km s^{-1}). The contour levels are at 3σ , 4σ , and 5σ (where $1\sigma = 2.8 \times 10^{-3}\text{ Jy beam}^{-1}\text{ km s}^{-1}$). Panel (d): 82 GHz continuum emission (color) overlaid with the integrated intensity emission map of the $c\text{-C}_3\text{H}_2$ ($3_{1,2}\text{--}3_{0,3}$) at 82,966 MHz (black contours). The contour levels for the continuum and $c\text{-C}_3\text{H}_2$ emission maps are the same as those in Fontani et al. (2017) and in panel (b). Finally, in panels (a), (b), (c), and (d), the black triangles indicate the positions of the FIR3, FIR4, and FIR5 regions (see Chini et al. 1997); and the blue circle shows the NOEMA field of view.

$c\text{-C}_3\text{H}_2$ line emission is detected around FIR4, while FIR 3 and FIR5 do not show any emission above the 3σ level. The emission at 82 GHz toward FIR4 is rather extended with a hint that it could be associated with two compact sources northwest and southeast of FIR4, respectively. The map at 85 GHz, obtained with a higher spatial resolution, reveals emission in the same region as the one seen with the 82 GHz lines. Again, the emission is slightly clumpy (with 1σ difference between clumps). A forthcoming study, using higher spatial resolution continuum observations will address the level of core fragmentation in detail (R. Neri et al. 2018, in preparation).

Interestingly enough, the extended $c\text{-C}_3\text{H}_2$ 82 GHz emission is roughly cospatial with that of HC_5N , (which was observed within the same frequency setting as that in Fontani et al. 2017), rather than that of HC_3N , as shown in Figure 2.

3.2. $c\text{-C}_3\text{H}_2$ Single-dish Emission

The 30 m observations detected 24 $c\text{-C}_3\text{H}_2$ lines, 14 from the ortho form and 10 from para. Spectra of the $c\text{-C}_3\text{H}_2$ transitions

observed with the IRAM 30 m telescope toward OMC-2 FIR 4 are displayed in Figures 8–10 in the Appendix. Their properties are reported in Table 2. The lines are peaked around the ambient cloud velocity ($\sim 11\text{ km s}^{-1}$) and are narrow ($\text{FWHM} \sim 1.0\text{--}1.6\text{ km s}^{-1}$), indicating that they are emitted by the dense envelope surrounding FIR4 (see Section 4).

3.3. Missing Flux

To estimate the fraction of the total flux that is filtered out in our interferometric data, we compared the NOEMA to the IRAM 30 m lines. More specifically, the NOEMA spectra were convolved with a Gaussian beam similar to that of the 30 m beam (i.e., $\sim 30''$ at 82–83 GHz). The convolution was performed at the central position of the IRAM 30 m observations (see Section 2). Finally, the IRAM-30 m spectra were smoothed to the same spectral resolution ($\sim 7.2\text{ km s}^{-1}$) as that of the NOEMA WideX spectra. The comparison of the integrated line fluxes shows that 57% of the $c\text{-C}_3\text{H}_2$ $2_{0,2}\text{--}1_{1,1}$ emission, 60% of that of $3_{1,2}\text{--}3_{0,3}$, and 80% of that of $2_{1,2}\text{--}1_{0,1}$ lines is resolved

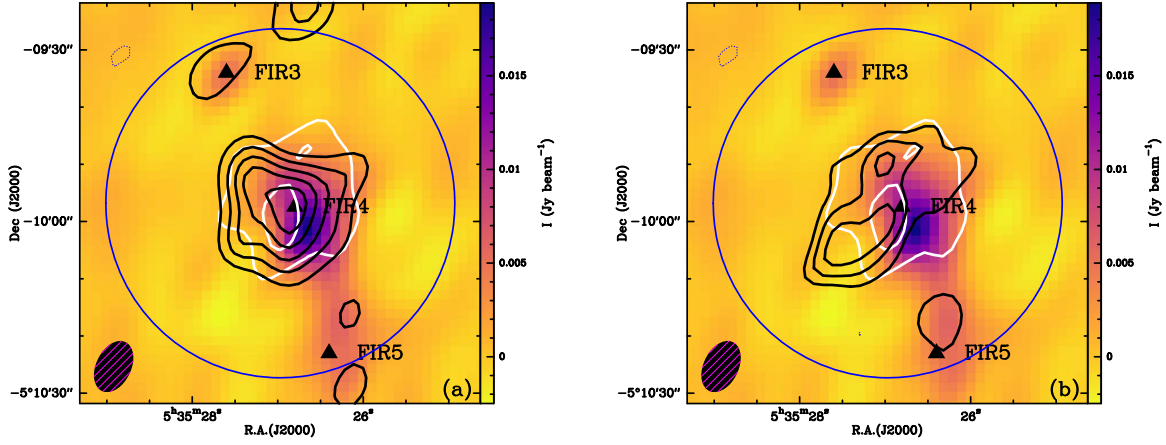


Figure 2. Panel (a): 82 GHz continuum emission (color) overlaid with the integrated intensity emission map of the $c\text{-C}_3\text{H}_2$ ($3_{1,2}\text{-}3_{0,3}$) at 82.97 GHz (white contours) and that of the HC_3N (9–8) at 81.88 GHz (black contours; from Fontani et al. 2017). Panel (b): 82 GHz continuum emission (color) overlaid with the integrated intensity emission map of the $c\text{-C}_3\text{H}_2$ ($3_{1,2}\text{-}3_{0,3}$) at 82.97 GHz (white contours) and that of the HC_3N (31–30) at 82.54 GHz (black contours; from Fontani et al. 2017). Finally, in panels (a) and (b), the contour levels for the continuum, HC_3N and HC_3N maps are the same as those in Fontani et al. (2017). Contour levels for the $c\text{-C}_3\text{H}_2$ emission map are given in Figure 1. The blue circle shows the NOEMA field of view.

Table 2
c- C_3H_2 Lines Detected with the IRAM 30 m Telescope

Freq. (GHz)	E_{up} (K)	A (10^{-5} s^{-1})	Intensity ^a (K km s ⁻¹)	FWHM ^c (km s ⁻¹)
80.7232	28.8	1.5	0.058 ± 0.006	1.6
82.0936^b	6.4	2.1	0.310 ± 0.030	1.6
82.9662^b	16.0	1.1	0.290 ± 0.030	1.5
84.7277	16.1	1.2	0.100 ± 0.010	1.5
85.3389^b	6.4	2.6	1.200 ± 0.120	1.4
85.6564	29.1	1.7	0.120 ± 0.010	1.4
150.4365	9.7	5.9	0.240 ± 0.050	1.2
150.8207	19.3	18.0	0.590 ± 0.120	1.2
150.8519	19.3	18.0	1.700 ± 0.340	1.2
151.0392	54.7	6.9	0.043 ± 0.009	1.1
151.3439	35.4	4.4	0.110 ± 0.020	1.1
151.3611	35.4	4.4	0.042 ± 0.008	1.1
155.5183	16.1	12.3	0.400 ± 0.080	1.1
204.7889	28.8	13.7	0.130 ± 0.030	1.1
216.2788	19.5	28.1	0.740 ± 0.150	1.0
217.8221	38.6	59.3	1.360 ± 0.270	1.2
217.9400	35.4	44.3	0.700 ± 0.140	1.1
218.1604	35.4	44.4	0.270 ± 0.050	1.1
227.1691	29.1	34.2	0.630 ± 0.120	1.0
244.2221	18.2	6.5	0.230 ± 0.050	1.2
249.0544	41.0	45.7	0.280 ± 0.060	1.1
251.3143	50.7	93.5	0.870 ± 0.170	1.2
254.9876	41.1	51.7	0.120 ± 0.020	1.0
260.4797	44.7	17.7	0.080 ± 0.020	1.1

Notes. We used the spectroscopic data parameters from Bogey et al. (1986), Vrtilek et al. (1987), Lovas et al. (1992), and Spezzano et al. (2012), that are available from the Cologne Database for Molecular Spectroscopy molecular line catalog (CDMS, Müller et al. 2005). The Einstein coefficients assume an ortho-to-para ratio of 3:1. The bold values show the transitions that have also been observed with NOEMA as part of the SOLIS program (see Table 1).

^a The error in the intensity is the quadratic sum of the statistical and calibration errors.

^b The emission from this line was imaged by NOEMA.

^c The FWHM result from Gaussian fit.

out. Therefore, the $c\text{-C}_3\text{H}_2$ emission detected by NOEMA very likely probes the densest part of the envelope surrounding FIR4 and not the ambient cloud.

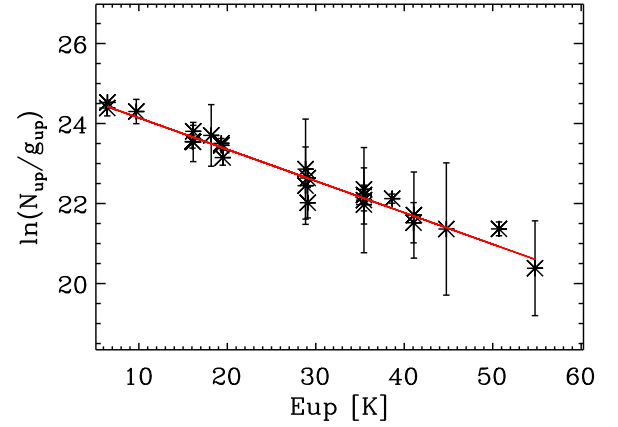


Figure 3. Rotational diagram derived from the $c\text{-C}_3\text{H}_2$ lines detected with the IRAM 30 m telescope (Table 2). The ortho-to-para ratio is taken equal to 3. The error bars correspond to the 1σ Gaussian fit uncertainties.

4. Temperature and $c\text{-C}_3\text{H}_2$ Column Density

4.1. Average Properties of the FIR4 Envelope

We first derive the average properties of the FIR4 envelope using the IRAM 30 m data. To this end, we first carried out a simple LTE analysis, and then a non-LTE one.

4.1.1. LTE Analysis

The rotational diagram, obtained assuming an ortho-to-para ratio equal to 3 and a beam filling factor equal to 1, is shown in Figure 3. No systematic difference is seen between ortho and para lines, which implies that our assumption on the ortho-to-para ratio is basically correct.

The derived rotational temperature is (12.6 ± 0.5) K and the $c\text{-C}_3\text{H}_2$ column density is $(7 \pm 1) \times 10^{12} \text{ cm}^{-2}$. Assuming that the emission arises from a $20''$ region (see below), would not change these results much: it would give (10.7 ± 0.5) K and $(1.5 \pm 0.2) \times 10^{13} \text{ cm}^{-2}$, respectively, and a slightly worse (but not significantly better) χ^2_{red} (0.08 instead of 0.05).

4.1.2. non-LTE Analysis

Given the large number of $c\text{-C}_3\text{H}_2$ lines, we carried out a non-LTE analysis assuming the Large Velocity Gradient (LVG) approximation. To this end, we used the LVG code described in Ceccarelli et al. (2002) and used the collisional coefficients with He, after scaling for the different mass of H_2 , computed by Chandra & Kegel (2000) and retrieved from the BASECOL database.¹⁵ We assumed a $c\text{-C}_3\text{H}_2$ ortho-to-para ratio equal to 3, as suggested by the LTE analysis.

We ran a large grid of models with H_2 density between 3×10^4 and $5 \times 10^6 \text{ cm}^{-3}$, temperature between 10 and 50 K, and $c\text{-C}_3\text{H}_2$ column density between 3×10^{12} and $2 \times 10^{13} \text{ cm}^{-2}$. We adopted an FWHM of 1.3 km s^{-1} and let the filling factor be a free parameter. We then compared the LVG predictions with the observations and used the standard minimum reduced χ^2 criterium to constrain the four parameters: H_2 density, temperature, column density, and size. In practice, for each column density, we found the minimum χ^2 in the density–temperature–size parameter space. The solution then is the one with the $c\text{-C}_3\text{H}_2$ column density giving the smallest χ^2 .

The best fit is obtained for an extended source (i.e., $\geq 30''$), $c\text{-C}_3\text{H}_2$ column density equal to $(7 \pm 1) \times 10^{12} \text{ cm}^{-2}$ (in excellent agreement with the LTE estimate), temperature equal to 40 K and density equal to $3 \times 10^5 \text{ cm}^{-3}$. At the 2σ level, the solution becomes degenerate in the density–temperature parameter space. A family of solutions is possible, with the two extremes at 15 K and $5 \times 10^6 \text{ cm}^{-3}$ on one side, and 50 K and $2 \times 10^5 \text{ cm}^{-3}$ on the other side. Please note that, indeed, the coldest and densest solution provides a temperature close to the rotational temperature (13 K). This means that the apparent LTE distribution of the transition levels derived by the IRAM 30 m line intensities is also obtained with non-LTE conditions and the densities and temperatures mentioned above, included the best-fit solution. Finally, in all cases, the lines are optically thin. In the following, we will use the best-fit solution and we will associate the errors as follows: $(40 \pm 10) \text{ K}$ and $(3 \pm 1) \times 10^5 \text{ cm}^{-3}$.

Assuming a H_2 column density measured from the continuum by Fontani et al. (2017), $\sim 10^{24} \text{ cm}^{-2}$, we obtain an average $c\text{-C}_3\text{H}_2$ abundance of $(7 \pm 1) \times 10^{-12}$, assuming that $c\text{-C}_3\text{H}_2$ is present across the entire OMC-2 FIR 4 region (Section 5).

4.2. The Structure of the FIR4 Envelope

The maps obtained with the NOEMA interferometer allow us to estimate the gas temperature and the $c\text{-C}_3\text{H}_2$ abundance across the region probed by the NOEMA observations.

To measure the excitation temperature, we use the two $c\text{-C}_3\text{H}_2$ lines at 82 GHz, which have the same spatial resolution and, most importantly, the same amount of filtered out extended emission.¹⁶ To this end, we assumed that (1) the $c\text{-C}_3\text{H}_2$ ortho-to-para ratio is equal to 3, (2) the lines are optically thin, and (3) the levels are LTE populated. With this assumptions, we derived the excitation temperature map shown in Figure 4, along with the associated uncertainty. The excitation temperature is comprised between 8 ± 3 and $16 \pm 7 \text{ K}$ (i.e., minimum and maximum values, see Figure 4). When considering the uncertainty on the

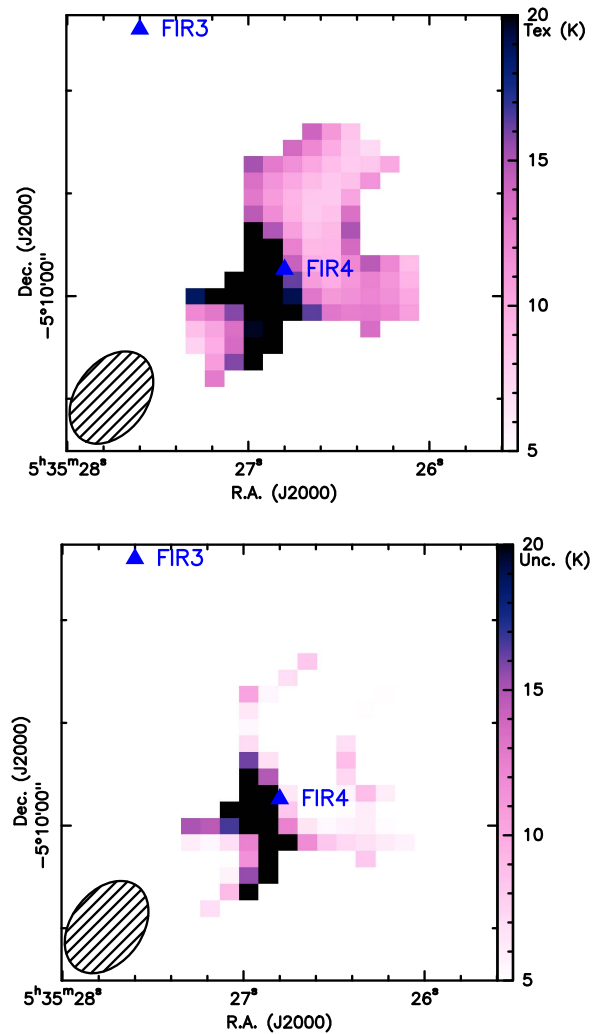


Figure 4. $c\text{-C}_3\text{H}_2$ excitation temperature map toward OMC2–FIR4 (top panel) along with the uncertainty map (bottom panel).

values, there are no signs of excitation temperature gradients across the region we are probing (about 3–4 beams). On the contrary, the excitation temperature seems to be rather constant and not much different from that probed by the 30 m data analysis ($\sim 12 \text{ K}$) (see the previous section).

5. Chemical Modeling

In the previous section, we showed that the gas emitting the $c\text{-C}_3\text{H}_2$ lines has a temperature of $\sim 40 \text{ K}$ and H_2 density $\sim 3 \times 10^5 \text{ cm}^{-3}$. The $c\text{-C}_3\text{H}_2$ column density is $\sim 7 \times 10^{12} \text{ cm}^{-2}$. In this section, we use a Photo-Dissociation Region (PDR) model to understand the structure of the gas probed by the $c\text{-C}_3\text{H}_2$ lines, notably where they come from, and what constraints they provide.

To this end, we used the Meudon PDR code¹⁷ (version 1.5.2, see Le Petit et al. 2006; Bron et al. 2016). The code computes the steady-state thermal and chemical structure of a cloud irradiated by an FUV radiation field G_0 and permeated by CR that ionize the gas at a rate ζ_{CR} . Relevant to the chemistry, the code computes the gas-phase abundances of the most abundant

¹⁵ <http://basecol.obspm.fr>: Dubernet et al. (2013).

¹⁶ Please note that the 85 GHz line has a filtering twice larger than that of the lines at 82 GHz (Section 3.3).

¹⁷ The code is publicly available at <http://pdr.obspm.fr>.

Table 3
Assumed Elementary Abundances, with Respect
to H Nuclei, in the PDR Modeling

Element	Abundance	Element	Abundance
O	3.2×10^{-4}	C	1.3×10^{-4}
N	7.5×10^{-5}	S	1.9×10^{-5}
Si	8.2×10^{-7}	Fe	1.5×10^{-8}

species, including $c\text{-C}_3\text{H}_2$. In our simulations, we adopted the density derived by the $c\text{-C}_3\text{H}_2$ non-LTE analysis ($n_{\text{H}} = 6 \times 10^5 \text{ cm}^{-3}$) and the elemental abundances listed in Table 3. Note that we limited the PDR simulations to a H-nuclei column density N_{H} of $\sim 4 \times 10^{22} \text{ cm}^{-2}$ (corresponding to $A_{\text{v}} = 20$ mag; see Figures 5 and 6). However, to compare the final predicted $c\text{-C}_3\text{H}_2$ column density, N_{Tot} , with the observed one ($7 \times 10^{12} \text{ cm}^{-2}$), we have to consider the whole cloud, which has a total H-nuclei column density $N_{\text{H}}^{\text{FIR4}}$ of $2 \times 10^{24} \text{ cm}^{-2}$ (Fontani et al. 2017). Therefore, we multiplied the $c\text{-C}_3\text{H}_2$ abundance predicted by the model in the cloud interior X_{interior} (computed by the code at $N_{\text{H}} = 3 \times 10^{22} \text{ cm}^{-2}$)¹⁸ by $N_{\text{H}}^{\text{FIR4}}$, and added it to the $c\text{-C}_3\text{H}_2$ column density in the PDR region N_{PDR} (computed by the code for $N_{\text{H}} \leq 1 \times 10^{22} \text{ cm}^{-2}$), as follows:

$$N_{\text{Tot}} = X_{\text{interior}} \times N_{\text{H}}^{\text{FIR4}} + 2 \times N_{\text{PDR}}. \quad (1)$$

To initialize our grid of models, we used as input parameter a temperature of 50 K, and assume an edge-on region that is irradiated from one side only. Then, we run several models with values of G_0 (G_0 is the FUV radiation field in Habing units¹⁹) ranging from 1 to 1700, and ζ_{CR} from $1 \times 10^{-16} \text{ s}^{-1}$ to $4 \times 10^{-14} \text{ s}^{-1}$. These extreme values are quoted in the literature for the OMC-2 region (see the Introduction and Discussion). Note that, even though we did not run a full grid of models, we fine-tuned the parameter ranges close to the best-fit solution.

The run models and the associated results are listed in Table 4 and shown in Figure 5. Both the predicted $c\text{-C}_3\text{H}_2$ column density and gas temperature are strong functions of ζ_{CR} : the larger ζ_{CR} the larger the column density and the temperature. On the contrary, the value of G_0 has a small influence on the predicted values, in particular, for the temperature.

The comparison of the PDR modeling results (Table 4 and Figure 5) with the measured $c\text{-C}_3\text{H}_2$ column density and gas temperature very clearly indicates that the gas is permeated by a large flux of CR and is irradiated by an intense FUV field. Specifically, model 12 ($\zeta_{\text{CR}} = 4 \times 10^{-14} \text{ s}^{-1}$ and $G_0 = 1700$) reproduces fairly well the measured $c\text{-C}_3\text{H}_2$ column density ($\sim 7 \times 10^{12} \text{ cm}^{-2}$) and gas temperature ($\sim 40 \text{ K}$).

Figure 6 shows the gas temperature, the $c\text{-C}_3\text{H}_2$ abundance, and column density as a function of $N(\text{H}+2 \times \text{H}_2)$ for model 12, which best reproduces the observations, and model 2, for comparison.

In general, the $c\text{-C}_3\text{H}_2$ abundance has a first peak in the PDR region, in a tiny layer at $N(\text{H}+2 \times \text{H}_2) \leq 10^{21} \text{ cm}^{-2}$. This first peak depends on the FUV radiation field and increases with increasing G_0 . In the interior of the cloud, at $N(\text{H}+2 \times \text{H}_2)$

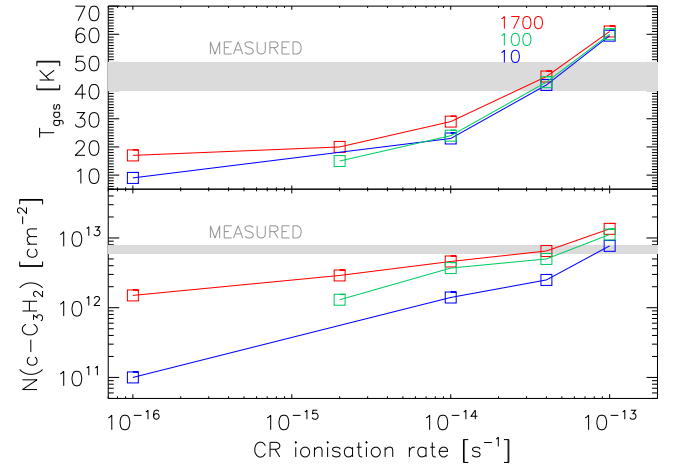


Figure 5. Results of the PDR modeling: predicted $c\text{-C}_3\text{H}_2$ column density (lower panel) and gas temperature (upper panel) as a function of the CR ionization rate ζ_{CR} , for an FUV field G_0 equal to 1700 (red), 100 (green), and 10 (blue), respectively. Symbols show the actual runs.

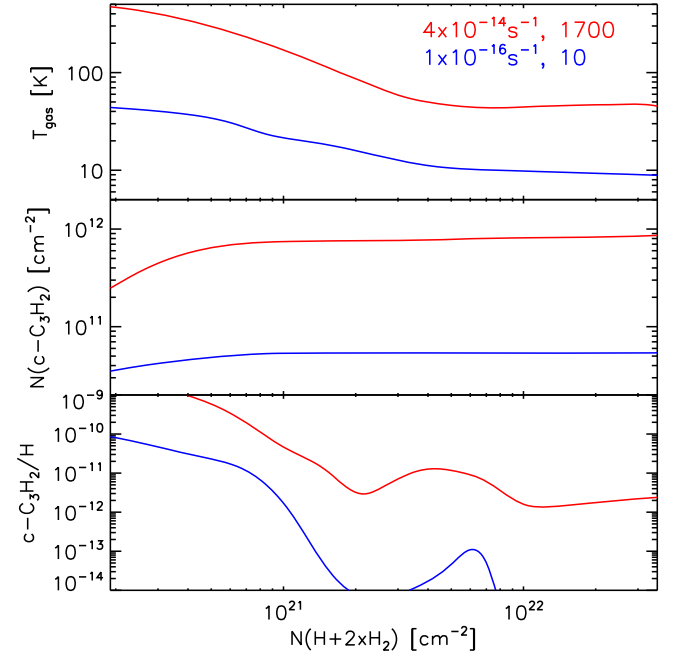


Figure 6. Thermal and chemical structure of two models: predicted gas temperature (upper panel), $c\text{-C}_3\text{H}_2$ column density in the PDR (middle panel), and abundance (bottom panel) as a function of the H nuclei column density. Two models are reported: model 12 ($\zeta_{\text{CR}} = 4 \times 10^{-14} \text{ s}^{-1}$ and $G_0 = 1700$; red), and model 2 ($\zeta_{\text{CR}} = 1 \times 10^{-16} \text{ s}^{-1}$ and $G_0 = 10$; blue).

$\geq 10^{22} \text{ cm}^{-2}$, namely in the region that contributes most to the total $c\text{-C}_3\text{H}_2$ column density, the $c\text{-C}_3\text{H}_2$ abundance is governed by the CR ionization rate and increases with ζ_{CR} . As expected, the gas temperature at the PDR border is governed by the FUV field, whereas it is governed by CR ionization rate in the interior.

6. Discussion

6.1. OMC-2 FIR 4: A Highly Irradiated Region

In the previous section, we showed that in order to reproduce the temperature of the gas probed by the $c\text{-C}_3\text{H}_2$ lines and its

¹⁸ Please note that we used the $c\text{-C}_3\text{H}_2$ abundance at $N_{\text{H}} = 3 \times 10^{22} \text{ cm}^{-2}$ to avoid the region where opacities and, consequently, temperatures decrease because of the artificial boundary of the cloud.

¹⁹ $G_0 = 1$ corresponds to an FUV energy density of $5.3 \times 10^{-14} \text{ erg cm}^{-2} \text{ s}^{-1}$. The interstellar standard radiation field is $G_0 = 1.7$.

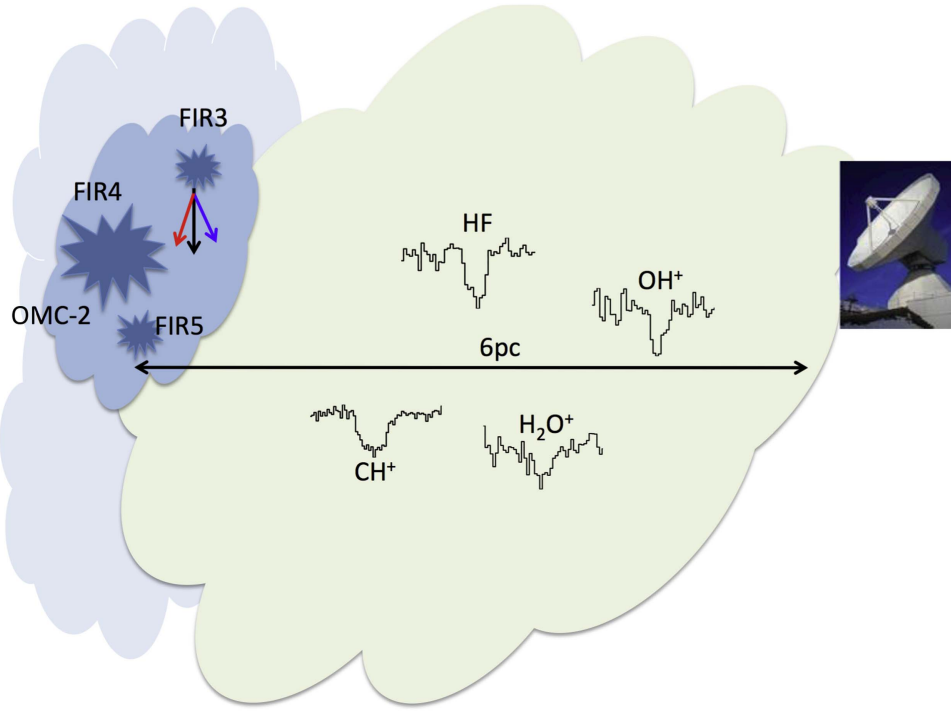


Figure 7. Cartoon of OMC-2. A tenuous cloud between OMC-2 and the Sun is probed by the absorption of HF, OH⁺, CH⁺, and H₂O⁺ observed by the Herschel HIFI instrument (López-Sepulcre et al. 2013a). The OMC-2 complex is associated with three FIR sources: FIR3, FIR4, and FIR5, respectively. An outflow is emitted by FIR3 which, based on the present observations, is unlikely impacting the FIR4 envelope.

Table 4

List of the ζ_{CR} and G_0 Values Adopted for the Different PDR Models and the Results of the Simulations: the c-C₃H₂ Column Density in the PDR Region, N_{PDR} ; the c-C₃H₂ Abundance (with Respect to H Nuclei) in the Interior (See the Text), X_{interior} ; the Total c-C₃H₂ Column Density, N_{Tot} , which Takes into Account the Whole Cloud (See the Text); the Gas Temperature (in the Interior)

Model	ζ_{CR} (10^{-16} s^{-1})	G_0	N_{PDR} (10^{12} cm^{-2})	X_{interior}	N_{Tot} (10^{12} cm^{-2})	T_{gas} (K)
1	1	1	0.01	9.8×10^{-16}	0.02	9
2	1	10	0.05	1.5×10^{-15}	0.1	9
3	1	1700	0.75	2.5×10^{-14}	1.5	17
4	20	100	0.11	5.3×10^{-13}	1.3	14
5	20	1700	0.77	7.1×10^{-13}	2.9	20
6	100	10	0.12	5.7×10^{-13}	1.4	23
7	100	100	0.18	1.6×10^{-12}	3.7	25
8	100	1700	0.79	1.5×10^{-12}	4.6	29
9	400	1	0.06	7.4×10^{-13}	1.6	41
10	400	10	0.19	1.1×10^{-12}	2.5	42
11	400	100	0.26	2.2×10^{-12}	5.0	43
12	400	1700	0.86	2.4×10^{-12}	6.5	45

abundance the gas has to be irradiated by a strong flux of CR-like particles. Amazingly, the best agreement between observations and model predictions is given by a CR ionization rate, $\zeta_{\text{CR}} = 4 \times 10^{-14} \text{ s}^{-1}$, that is the same as the one derived by the following observations: (1) the HCO⁺ and N₂H⁺ high J lines observed by Herschel HIFI CHESS project (Ceccarelli et al. 2014), and (2) the HC₃N and HC₅N lines observed by the NOEMA SOLIS project (Fontani et al. 2017). In addition, the c-C₃H₂ emitting region roughly coincides with the largest ζ_{CR} region that is probed by the HC₅N emission area. We emphasize that, in addition to being different data sets and different species, the three estimates of ζ_{CR} have been obtained

also with three different astrochemical codes: ASTRO-CHEM,²⁰ Nahoon (Wakelam et al. 2012) and Meudon PDR (version 1.5.2, Bron et al. 2016; Le Petit et al. 2006) codes.

The emerging picture is shown in the cartoon of Figure 7. Previous Herschel HIFI CHESS observations showed that between OMC-2 and us there is a tenuous (100 cm^{-3}) cloud extending about 6 pc along the line of sight, and illuminated by an FUV field about 1000 times brighter than the interstellar standard radiation field (López-Sepulcre et al. 2013a). OMC-2 itself hosts three FIR sources (FIR 3–5), which are likely very

²⁰ <http://smaret.github.com/astrochem/>

different in nature and evolutionary status, even though not much is known, especially about FIR3 and FIR5, except that a large-scale ($\sim 30''$) outflow emanates from FIR3 (Shimajiri et al. 2008, 2015; Takahashi et al. 2008). FIR4 is actually a dense clump ($\sim 10^5$ – 10^6 cm $^{-3}$; Crimier et al. 2009; Ceccarelli et al. 2014) with an embedded cluster of young sources, whose number is still unclear (Shimajiri et al. 2008; López-Sepulcre et al. 2013b; Kainulainen et al. 2017). What is clear now is that FIR4 is permeated by a flux of CR-like ionizing particles about 1000 times larger than the CR flux of the Galaxy. The source(s) of these particles is(are) likely situated in the east part of FIR4 (Fontani et al. 2017), but still remain(s) unidentified. Incidentally, it is important to note that the high CR ionization rate could result in a temperature gradient in the vicinity of the CR emitting source(s). Nonetheless, the c-C₃H₂ excitation temperature mainly covers the west region (see Figure 4), where the irradiation is likely lower, based on the HC₅N/HC₃N abundance ratio by Fontani et al. (2017). The new IRAM 30 m and SOLIS observations presented in this work confirm this geometry and indicate that abundant hydrocarbons (c-C₃H₂) are present not only at the skin of the FIR4 clump but also in the interior, because of the strong CR-like irradiation.

6.2. No Evidence of the FIR3 Outflow Impact on FIR4

It has been suggested that the chemical composition of OMC-2 FIR4 is affected by the interaction of the northeast–southwest outflow driven by the nearby source FIR3 (see Shimajiri et al. 2008, 2015), which is located at about 23'' northeast from FIR4 (i.e., ~ 9660 au at a distance of 420 pc; Hirota et al. 2007; Menten et al. 2007). Specifically, Shimajiri et al. (2008, 2015) have suggested that gas associated with OMC-2 FIR4 might be impacted by this NE–SW outflow. If this is the case, the gas associated with the envelope of the OMC-2 FIR4 region should show some physically induced effect. In this instance, the c-C₃H₂ molecular emission map would likely present a temperature gradient within the region. This is not the case in our observations (see Figure 4) which, contrary to Shimajiri et al. (2015), probe the envelope of OMC-2 FIR4 and not the ambient gas thanks to the interferometer spatial filtering. These findings lead one to ask whether the apparent spatial coincidence of the southern outflow lobe driven by FIR3 and the northern edge of FIR4 is simply a projection effect. More sensitive, higher angular resolution observations may help us confirm our current conclusion.

7. Conclusions

We have imaged, for the first time, the distribution of cyclopropenylidene, c-C₃H₂, toward OMC-2 FIR 4 with an angular resolution of $9''.5 \times 6''.1$ at 82 GHz and $4''.7 \times 2''.2$ at 85 GHz, using NOEMA. The observations were performed as part of the SOLIS program. In addition, we have performed a

study of the physical properties of this source through the use of IRAM-30 m observations.

Our main results and conclusions are the following:

1. From a non-LTE analysis of the IRAM-30 m data, we find that c-C₃H₂ gas emits at the average temperature of about 40 K with a $\chi(\text{c-C}_3\text{H}_2)$ abundance of $(7 \pm 1) \times 10^{-12}$.
2. Our NOEMA observations show that there is no sign of excitation temperature gradients within the observed region (which corresponds to ~ 3 – 4 beams), with a $T_{\text{ex}}(\text{c-C}_3\text{H}_2)$ in the range 8 ± 3 – 16 ± 7 K. Our findings suggest that the OMC-2 FIR 4 envelope is not in direct physical interaction with the outflow originating from OMC-2 FIR 3.
3. In addition, the c-C₃H₂ gas probed by NOEMA arises from the same region as that of HC₅N which is a probe of high CR-particles ionization (Fontani et al. 2017).
4. Finally, a notable result, derived from chemical modeling with the Meudon PDR code is that OMC-2 FIR 4 appears to be a strongly irradiated region: FUV field dominates the outer shells (with a radiation field scaling factor G_0 of about 1700), while the interior of the envelope is governed by CR ionization (with a CR ionization rate $\zeta_{\text{CR}} = 4 \times 10^{-14}$ s $^{-1}$, namely more than a thousand times the canonical value).

These results are consistent with previous studies claiming that OMC-2 FIR 4 bathes in an intense radiation field of energetic particles (≥ 10 MeV).

We acknowledge the anonymous referee for fruitful comments. We warmly thank Franck Le Petit for his assistance in the use of the PDR code. C.F. acknowledges the financial support for this work provided by the French space agency CNES along with the support from the Italian Ministry of Education, Universities and Research, project SIR (RBSI14ZRHR). We acknowledge the funding from the European Research Council (ERC), projects PALs (contract 320620) and DOC (contract 741002). This work was supported by the French program Physique et Chimie du Milieu Interstellaire (PCMI) funded by the Conseil National de la Recherche Scientifique (CNRS) and Centre National d’Etudes Spatiales (CNES) and by the Italian Ministero dell’Istruzione, Università e Ricerca through the grant Progetti Premiali 2012—iALMA (CUP C52I13000140001).

Appendix

c-C₃H₂ toward OMC-2 FIR 4 as Observed with the IRAM-30 m Telescope

Figures 8–10 display the spectra of the c-C₃H₂ transitions observed with the IRAM 30 m telescope toward OMC-2 FIR 4 at 1, 2, and 3 mm, respectively.

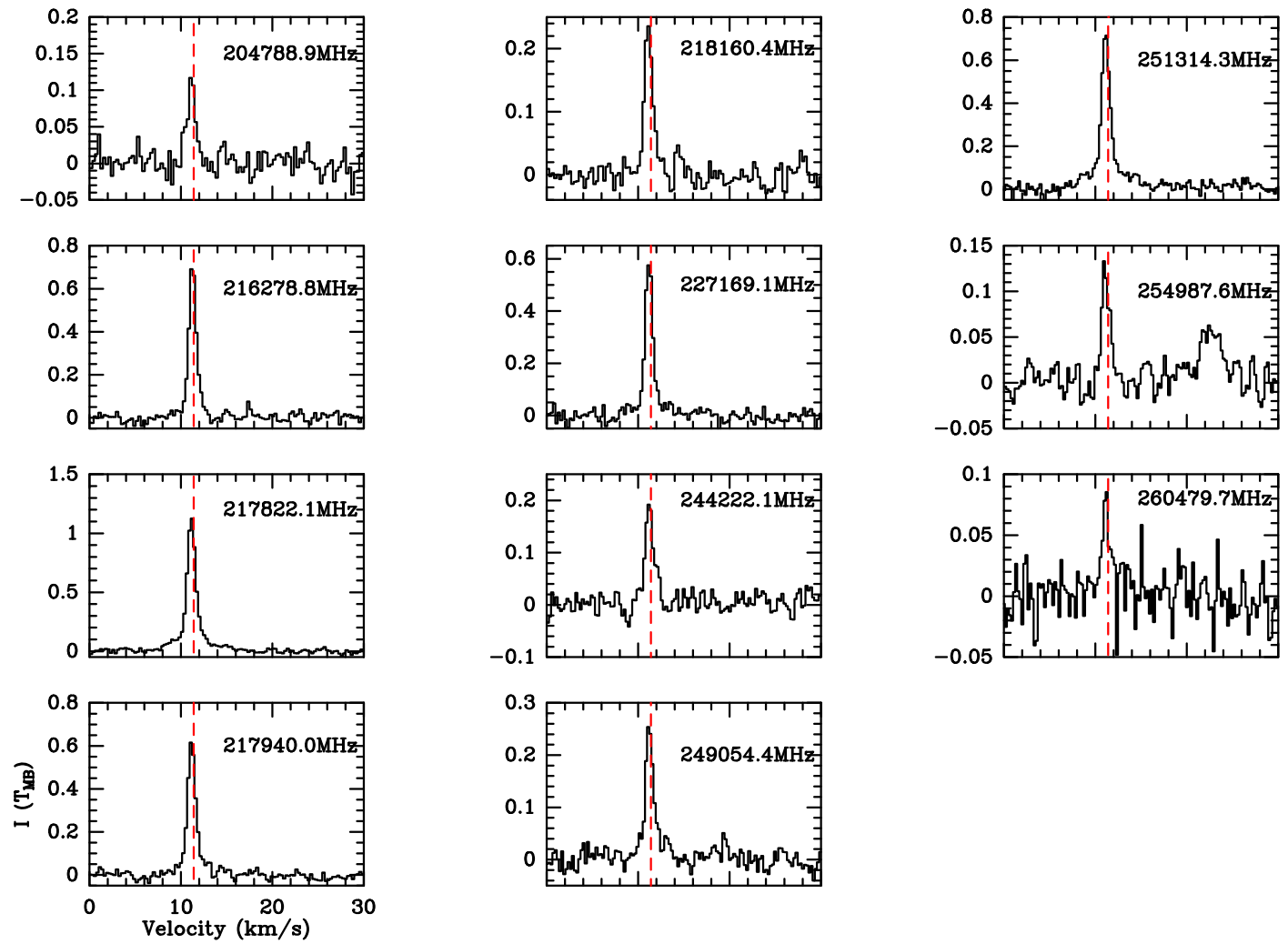


Figure 8. $c\text{-C}_3\text{H}_2$ spectra observed toward OMC-2 FIR 4 at 1 mm with the IRAM 30 m telescope. Dashed red lines indicate a $V_{\text{LSR}} = 11.4 \text{ km s}^{-1}$. The frequency of the observed transition is indicated on each plot.

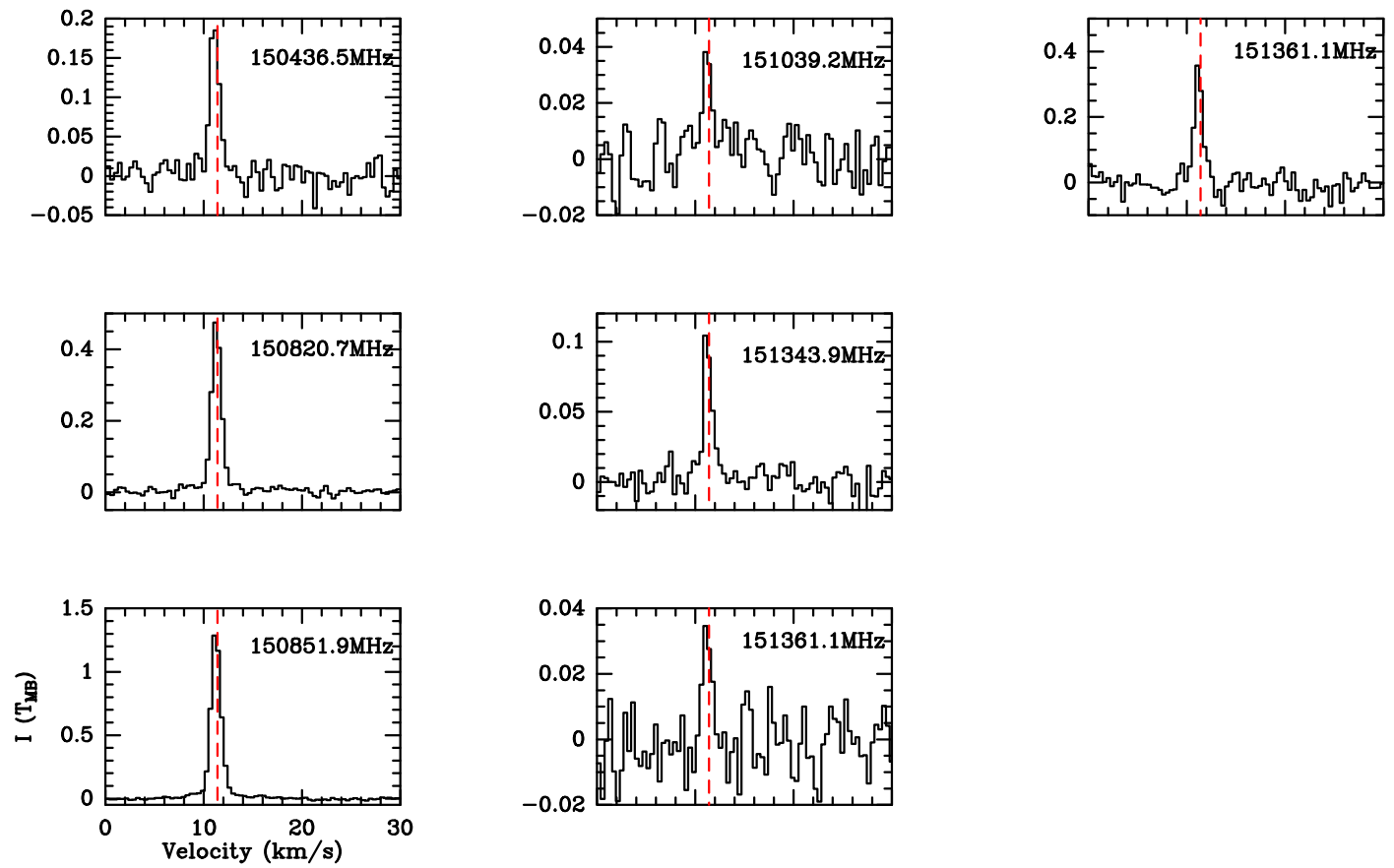


Figure 9. $c\text{-C}_3\text{H}_2$ spectra observed toward OMC-2 FIR 4 at 2 mm with the IRAM 30 m telescope. Dashed red lines indicate a $V_{\text{LSR}} = 11.4 \text{ km s}^{-1}$. The frequency of the observed transition is indicated on each plot.

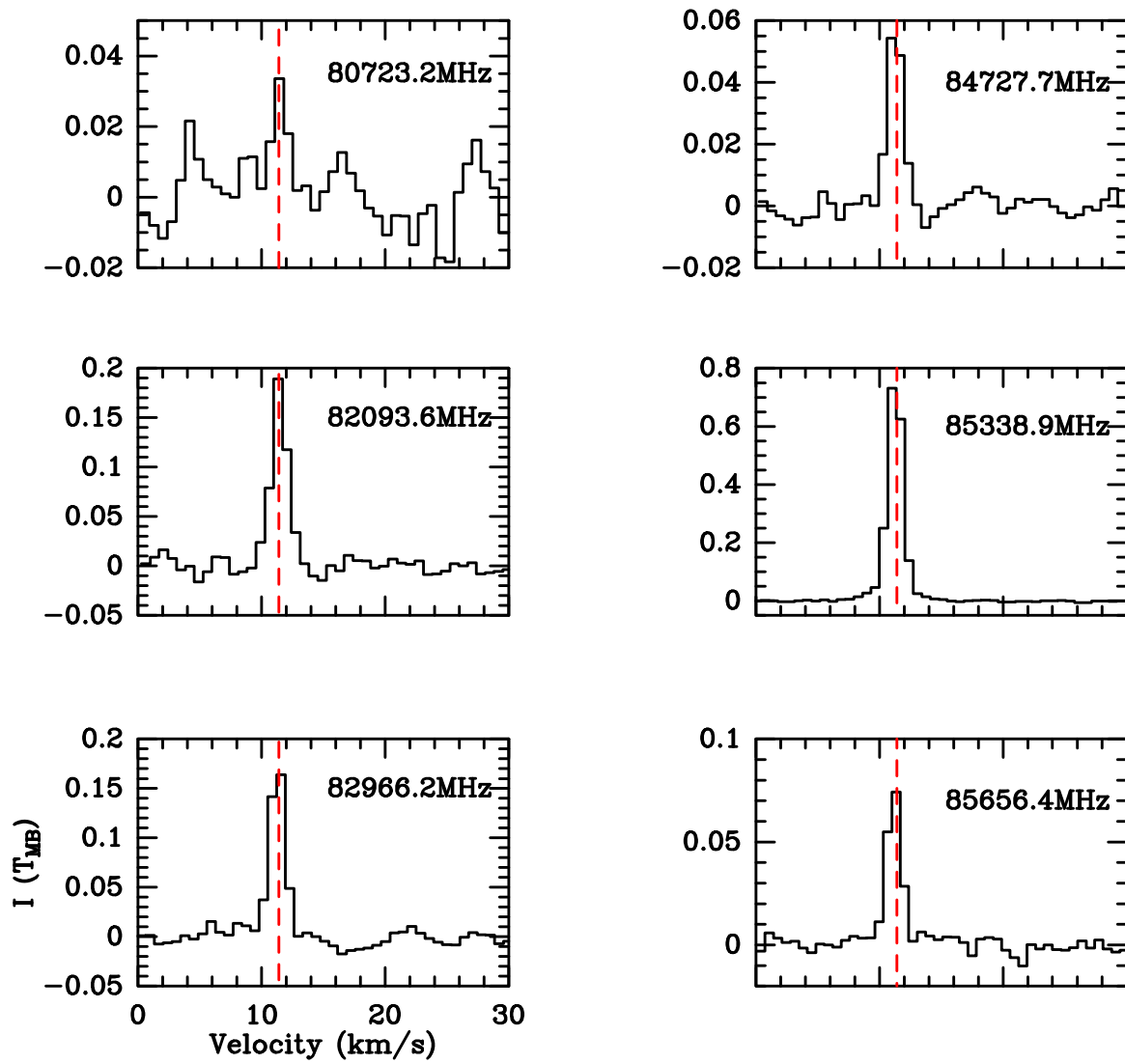









Figure 10. $c\text{-C}_3\text{H}_2$ spectra observed toward OMC-2 FIR 4 at 3 mm with the IRAM 30 m telescope. Dashed red lines indicate a $V_{\text{LSR}} = 11.4 \text{ km s}^{-1}$. The frequency of the observed transition is indicated on each plot.

ORCID iDs

C. Favre  <https://orcid.org/0000-0002-5789-6931>
 C. Ceccarelli  <https://orcid.org/0000-0001-9664-6292>
 A. López-Sepulcre  <https://orcid.org/0000-0002-6729-3640>
 F. Fontani  <https://orcid.org/0000-0003-0348-3418>
 R. Neri  <https://orcid.org/0000-0002-7176-4046>
 P. Caselli  <https://orcid.org/0000-0003-1481-7911>
 C. Kahane  <https://orcid.org/0000-0003-1691-4686>
 F. Alves  <https://orcid.org/0000-0002-7945-064X>
 N. Balucani  <https://orcid.org/0000-0001-5121-5683>
 C. Codella  <https://orcid.org/0000-0003-1514-3074>
 J. E. Pineda  <https://orcid.org/0000-0002-3972-1978>

References

- Adams, F. C. 2010, *ARA&A*, **48**, 47
 Bogey, M., Demuynck, C., & Destombes, J. L. 1986, *CPL*, **125**, 383
 Bron, E., Le Petit, F., & Le Bourlot, J. 2016, *A&A*, **588**, A27
 Caselli, P., & Ceccarelli, C. 2012, *A&ARv*, **20**, 56
 Ceccarelli, C., Baluteau, J.-P., Walmsley, M., et al. 2002, *A&A*, **383**, 603
 Ceccarelli, C., Caselli, P., Fontani, F., et al. 2017, *ApJ*, **850**, 176
 Ceccarelli, C., Dominik, C., López-Sepulcre, A., et al. 2014, *ApJL*, **790**, L1
 Chandra, S., & Kegel, W. H. 2000, *A&AS*, **142**, 113
 Chini, R., Reipurth, B., Ward-Thompson, D., et al. 1997, *ApJL*, **474**, L135
 Crimier, N., Ceccarelli, C., Lefloch, B., & Faure, A. 2009, *A&A*, **506**, 1229
 Dubernet, M.-L., Alexander, M. H., Ba, Y. A., et al. 2013, *A&A*, **553**, A50
 Fontani, F., Ceccarelli, C., Favre, C., et al. 2017, *A&A*, **605**, A57
 Gounelle, M., Chaussidon, M., & Rollier-Bard, C. 2013, *ApJL*, **763**, L33
 Hirota, T., Bushimata, T., Choi, Y. K., et al. 2007, *PASJ*, **59**, 897
 Högbom, J. A. 1974, *A&AS*, **15**, 417
 Kainulainen, J., Stutz, A. M., Stanke, T., et al. 2017, *A&A*, **600**, A141
 Le Petit, F., Nehmé, C., Le Bourlot, J., & Roueff, E. 2006, *ApJS*, **164**, 506
 López-Sepulcre, A., Jaber, A. A., Mendoza, E., et al. 2015, *MNRAS*, **449**, 2438
 López-Sepulcre, A., Kama, M., Ceccarelli, C., et al. 2013a, *A&A*, **549**, A114
 López-Sepulcre, A., Taquet, V., Sánchez-Monge, Á., et al. 2013b, *A&A*, **556**, A62
 Lovas, F. J., Suenram, R. D., Ogata, T., & Yamamoto, S. 1992, *ApJ*, **399**, 325
 Menten, K. M., Reid, M. J., Forbrich, J., & Brunthaler, A. 2007, *A&A*, **474**, 515
 Müller, H. S. P., Schlöder, F., Stutzki, J., & Winnewisser, G. 2005, *JMoSt*, **742**, 215
 Shimajiri, Y., Kawabe, R., Takakuwa, S., et al. 2011, *PASJ*, **63**, 105
 Shimajiri, Y., Sakai, T., Kitamura, Y., et al. 2015, *ApJS*, **221**, 31
 Shimajiri, Y., Takahashi, S., Takakuwa, S., Saito, M., & Kawabe, R. 2008, *ApJ*, **683**, 255
 Spezzano, S., Tamassia, F., Thorwirth, S., et al. 2012, *ApJS*, **200**, 1
 Takahashi, S., Saito, M., Ohashi, N., et al. 2008, *ApJ*, **688**, 344
 Vrtilik, J. M., Gottlieb, C. A., & Thaddeus, P. 1987, *ApJ*, **314**, 716
 Wakelam, V., Herbst, E., Loison, J.-C., et al. 2012, *ApJS*, **199**, 21